Composites: Part A 175 (2023) 107774

Contents lists available at ScienceDirect

Composites Part A

journal homepage: www.elsevier.com/locate/compositesa

Interlaminar Response of LSI-Produced C/SiC Ceramic Matrix Composites: Experiments and Modelling

Marco Riva [a,*], Alessandro Airoldi [a], Antonio Maria Caporale [a], Lorenzo Cavalli [b], Mario De Stefano Fumo [c]

[a] Department of Aerospace Science and Technology (DAER), Politecnico di Milano, Via La Masa, 34, 20156, Milan, Italy
[b] Petroceramics S.p.A, Viale Europa, 2, 24040 Stezzano (BG), Italy
[c] CIRA, Italian Aerospace Research Centre, Via Maiorise, 81043 Capua (CE), Italy

ARTICLE INFO

Keywords:
Ceramic-matrix composites (CMCs)
Delamination
Numerical analysis
Mechanical testing

ABSTRACT

This work investigates the interlaminar properties of a C/SiC composite produced by Liquid Silicon Infiltration, combining experiments based on Double Cantilever Beam tests and numerical analyses. Experimentally, a method to obtain pre-cracks with sharp tips at precise locations is proposed, and specimens with different thickness are used to investigate the effects of bending stress states in the delamination process. The properties of tri-linear Cohesive Zone Models for the modelling of delamination are identified numerically, by using automatic regression techniques without requiring additional assumptions or testing. Fiber bridging effects were observed and modelled, including the evaluation of the process zone lengths with different experimental, analytical, and numerical methods. Overall, the work provides a qualitative insight in the delamination process of long fiber reinforced C/SiC laminates produced with a cost-affordable technique and proposes an experimental and numerical protocol to characterize and model delamination phenomena, taking into account the scattering of material properties.

1. Introduction

Ceramic Matrix Composites (CMC) are a family of materials consisting of a refractory ceramic matrix toughened by long fibers, short fibers, or particles. They have gained increasing attention for their mechanical, thermal and tribological properties that are almost unique among all the material families. In fact, they combine good structural properties and several intrinsic toughening mechanisms with the capability to resist to abrasion, erosion, high temperatures, oxidation, and friction. Among the different refractory matrices, Silicon Carbide (SiC) stands out for the development of composites with high heat stability, superior strength at elevated temperatures and low density [1,2,3]. Composites based on Silicon Carbide toughened by carbon fibers (C/SiC composites) are well-known solutions for the development of thermal protections, hot structures, and parts of propulsive systems in the aerospace field [4,5,6]. CMCs are among the most promising candidates for reusable hot structures of space vehicles and propulsion systems, which involve the ability of withstanding several cycles of hyperthermal conditions while fulfilling primary structural roles without critical degradation.

The development of successful structural concepts in CMC materials depends crucially on their mechanical properties in severe environmental conditions and their costs. In general, their properties are strongly influenced by the manufacturing process adopted. Techniques based on Chemical Vapor Infiltration (CVI) and Polymer Infiltration and Pyrolysis (PIP) lead to a ceramic matrix with excellent qualities and avoid the presence of free silicon, but are characterized by elevated production costs, since they require high investments in facilities or expensive ceramic precursors, respectively [7]. It is worth remarking that such aspects represent nowadays a significant issue also in space applications, since reduction of production cost is fundamental for the next generation vehicles and for the future concept of space travel. However, the manufacturing costs of C/SiC composites saw a significant reduction when the Liquid Silicon Infiltration (LSI) technique was developed in DLR research center in Stuttgart, Germany [8]. This process consists of the infiltration of molten silicon into a preform of pyrolyzed polymeric matrix composite which reacts with the carbonaceous residual of the polymeric matrix, called pyrocarbon, to form a SiC phase.

* Corresponding author at: Department of Aerospace Science and Technology (DAER), Politecnico di Milano, Via La Masa, 34, 20156 Milano, Italy.
E-mail address: marco2.riva@polimi.it (M. Riva).

https://doi.org/10.1016/j.compositesa.2023.107774
Received 26 May 2023; Received in revised form 1 August 2023; Accepted 31 August 2023
Available online 3 September 2023

Unfortunately, this process can also lead to the partial siliconization of the carbon fibers, decreasing their load bearing capability [2,3]. In literature, several evolution models of the SiC phase were proposed [9,10,11] showing that different SiC phases are formed with dimensional order ranging from the nano- to the micro-scale. Considering the elevated infiltration temperature, the cooling process leads also to the presence of severe Thermal Residual Stresses (TRS) inside the material and to the formation of a network of fine cracks inside the matrix [2].

The inhomogeneity, the inherent presence of multiple failure modes, which is typical of composites, the role of thermal residual stress and the complex mechanical and chemical interactions between fiber and matrix complicate the application of CMC materials for structural applications, especially in the case of LSI-produced components. Accordingly, material characterization and modelling assume a fundamental importance in the design of cost-affordable CMC structures for reusable vehicles as well as for propulsive parts in conventional or innovative propulsion systems. In particular, the prediction of structural integrity and the development of damage tolerant structures requires a qualitative understanding of non-linear responses and failure mechanisms of the materials, reliable methods for the quantification of material properties, and analytical and numerical tools for the prediction of the structural response beyond the linear field.

Inelastic mechanisms and non-linear behavior are fundamental aspects of the response of CMC laminates, since they characterize the response in the plane of the laminae even in the low strain range. Such behavior has been studied by many works in literature (see for instance [12,13,14,15]). The intralaminar damage modes and more specifically delamination driven by out-of-plane stress fields are relatively less studied with respect to the extensive work performed on the characterization and modelling of in-plane behavior of CMC laminate. However, delamination can often occur in CMC under many circumstances. The residual stress states and the defects originated during the pyrolysis stage of manufacturing processes are a typical source for delamination onset [16]. Ply-drop offs in tapered specimens, curved laminates, and zone of static or dynamic transverse load applications can be subjected out-of-plane stress fields that can lead to delaminations in CMC as in polymer matrix composites [17,18,19].

These considerations highlight the importance of characterizing and modeling delamination phenomena for the development of reliable reusable CMC structures, although studying delamination in CMC involves several issues. One problem is related to the experimental characterization of the interlaminar toughness, which is typically measured in composites by using tests on pre-cracked specimens, as Double Cantilever Beam (DCB) and End Notched Flexure (ENF) tests. In CMC, the accomplishment of these tests and the interpretation of the results is complicated by the difficulties of obtaining pre-cracks with acceptable length, adequately sharp tips, and exactly positioned at the mid-plane of the specimens, since pre-cracking is typically carried out by sawing mechanically the specimens produced [20,21].

Other issues are represented by the dependency of the toughness on the crack length and by the scattering of data. Such phenomena have been documented, for instance, in works focused on desiliconized LSI-produced CMC, presented in [16,20]. Desiliconization eliminated the free silicon, thus leading to a critical operational condition, when melting temperature of silicon was exceeded in a re-entry space vehicle. The measures obtained from DCB tests indicated an R-curve effect on the interlaminar fracture toughness G_{Ic}, which was found to increase from 0.12 kJ/m^2 to 0.20 kJ/m^2 after a crack propagation of 20 mm, with a significant scattering. The increment of mode I interlaminar toughness with crack advancement was also found in DCB tests performed on the SiC/SiC composites produced through Polymer Infiltration and Pyrolysis (PIP) studied in [21], where a particularly remarkable R-curve effect was identified, and results were characterized by large scattering. In such work, the toughness levels were identified numerically through the adoption of a modelling technique based on Cohesive Zone Models with a tri-linear response, based on the technique developed in [22], for epoxy matrix carbon reinforced composites. A recent generalization of this technique adopted is presented in [23]. Sensitivity analyses performed on the model of DCB tests by using such numerical approach identified a toughness that varied from an initial value of about 0.018 kJ/m^2 to a final level of 0.508 kJ/m^2. Analogous results on a similar material were obtained in [24]. The high scattering registered in the force vs. displacement curves was attributed in [21] to the variation in the strength levels involved in the cohesive response of the interlaminar layers. Also, the presence of manufacturing defects, could be a reason for the scattering recorded in the characterization of the interlaminar toughness of this type of material [25].

A further problem is represented by the possible interaction between the delamination and damage occurring inside the ply due to the in-plane stress fields, which can arise during the progression of delamination tests, since, both in DCB and in ENF specimens, the arms of the pre-cracked coupons undergo significant bending. Such aspect was mentioned and studied numerically in [21] for a SiC/SiC CMC.

The activities in this paper are focused on LSI-produced C/SiC CMC presenting the experimental and numerical investigation on the mode I interlaminar crack propagation in LSI-produced DCB specimens, in the as built-state. The objectives of the work include the evaluation of methods to produce pre-cracks in the infiltration phase of the process, thus avoiding machining of the specimens and allowing to obtain a pre-crack with sharp tip in a precise interlaminar layer. The potential interactions between in-plane stress states and delamination are assessed both numerically and experimentally, by using specimens with different thickness and different in-plane stress levels during the DCB test and comparing the toughness measured. For the modelling of delamination, a numerical approach is adopted, based on the tri-linear CZM proposed by [22], like in [21], but applying a procedure for the automatic identification of the model parameters adopting as a guideline the procedure suggested in [26]. Both a regression model built by using a Neural Network combined with genetic algorithm optimization and a simpler Monte Carlo like method are used. This procedure does not require any assumptions on initial toughness and strength levels to identify the optimal model parameters for the correlation of force–displacement curves. Moreover, the automatic procedure is applied separately to each specimen, to identify the optimal material parameters for each test, so to correlate the scattering of the results with the distribution of model parameters and to propose method to evaluate an average set of parameters to calibrate the material models. Finally, the paper intends to provide a measure of the length of the fracture process zone, which will be referred also as damage zone, and to document fiber bridging effects by studying the surfaces of the crack faces after propagation. Overall, the work is aimed at improving the understanding of delamination phenomena in LSI-produced CMC laminates and at developing a complete and reliable experimental–numerical protocol for the characterization and the identification of their interlaminar toughness.

The paper is articulated in five sections, including this introduction. The following section covers the experimental testing procedure, where the interlaminar properties of the material are characterized by means of Double Cantilever Beam (DCB). These tests allowed to optimize the manufacturing process of pre-cracked specimens and to give a benchmark for the numerical procedure. Moreover, the section reports the results obtained for the material characterization in bending and in tension, with the development of an elastic plastic material model to approximately represent dissipative phenomena occurring in the bending response, which could affect the response of DCB test. The third section illustrates the numerical method exploited, which is characterized by the generation of a database of numerical responses, using SIMULIA/Abaqus environment, the implementation of a regression Neural Network, and the identification of the properties through a genetic algorithm-based optimization. In section four the method is assessed taking one specimen as benchmark, recognizing the drawbacks and the advantages of the method, and illustrating possible adjustments to the procedure to make it more effective. Finally, the last chapter

presents the results of the application of the procedure on all the specimens tested during the experimental campaign.

2. Experimental tests

2.1. General aspects of the test campaign

The subject of this study is a C/SiC composite material, manufactured through LSI technique by Petroceramics S.p.A. The structure of the composite is formed by a SiC matrix reinforced by a 2/2 twill of carbon fibers. The interlaminar characterization in mode I was carried out by performing DCB tests on pre-cracked C/SiC specimens. The test method used the ASTM standard D5528 [27] as a guideline, which was developed for polymer matrix composites with unidirectional reinforcement since neither a standard for fabric reinforced composites nor a specialized standard for ceramic matrix composites are available. The test, as exemplified in Fig. 1a, consists in the separation of the two arms of a pre-cracked specimen causing the crack to advance, while the force applied, the crack advancement, and the displacement of the two arms are measured. In this way is possible to evaluate the critical energy release rate, G_{Ic}, required for crack propagation. Such a measure can be carried out by applying different analytical and semi-analytical methods, as the ones proposed by the standard in [27], to evaluate the value of G_{Ic} from the force, the crack length and the displacement measured during the test. This work includes two DCB test campaigns performed on the same material. The differences between the two campaigns consist in the method to obtain the pre-crack, in the thickness of the DCB arms, and in the configurations of the hinges bonded to the specimen surfaces.

2.2. First DCB test campaign on the CMC material

In literature works, the pre-crack of DCB specimens has been obtained by machining the finished specimen interlamina with a diamond saw [16,20,21,24]. This technique is very simple, but it produces pre-cracks with blunt tips, typically significantly larger than ply thickness, with consequent uncertainties on the effective interface nature and with potential effect of the crack tip morphology over the results obtained in the first phases of crack propagation. In the present work, a method similar to the one used for polymeric matrix composites was applied. In a first attempt, a family of specimen was produced by inserting a polytetrafluoroethylene (PTFE) stripe inside the polymeric preform to keep the laminae separated in the precursor and to oppose to the siliconization of the pre-crack during the silicon infiltration, despite the very high temperature reached in this second process.

Four specimens were produced in this way with an average length of 152 mm, width of 12.41 ± 0.29 mm and thickness of 8.56 ± 0.28 mm. With this technique a maximum distance between the pre-crack tip and the edge of the specimens was of about 40 mm, which was obtained without any dimensional distortion of the specimens. The results, in terms of quality of the pre-crack, were not completely satisfactory. In fact, the thermal degradation of the PTFE stripe during the pyrolysis process allowed pure silicon to enter between the supposedly pre-cracked plies at discrete points, opposing to the complete development of the pre-crack. These accumulations were clearly visible by optical inspection on the side of the cut specimens, as show in Fig. 1b. Moreover, the presence of silicon complicated the measurement of the actual pre-crack length, which was estimated with an uncertainty of about ± 3 mm. A pair of steel hinges were attached to each specimen by using Araldite 2012 bicomponent epoxy. Considering the short distance between the edge and the crack tip, the length of the pre-crack was maximized by bonding hinges to the specimen surfaces as showed in Fig. 1a, obtaining a pre-crack length that could be estimated between 30 mm and 35 mm, as measured from the hinge center to the crack tip. The standard [27] prescribes the hinges to be bonded in the reversed configuration, which, in this case, would have led to an excessively short pre-crack length. In the configuration adopted, the flexural stiffness of the arms was influenced by the presence of the steel hinges, which dimensions were comparable to the pre-crack. However, the use of blocks or bonded tabs, indicated in [20,21], could have mitigated but not eliminated this effect, which is actually a consequence of the small pre-crack length. The free ends of the hinges were inserted in the grips of an MTS 858 testing machine, which was actuated in displacement control at a crosshead speed of 1 mm/min. The test system recorded the axial force and axial displacement with a frequency of 25 Hz. A graduated scale was drawn on one side of the specimens to allow a visual measure of the crack length evolution by using a high-definition camera, which was set to acquire a picture of the specimen every 5 s during the test. The camera and the testing machine were manually synchronized at the start of the test to be able to link the data acquired by the testing system to the crack length measured from the photos.

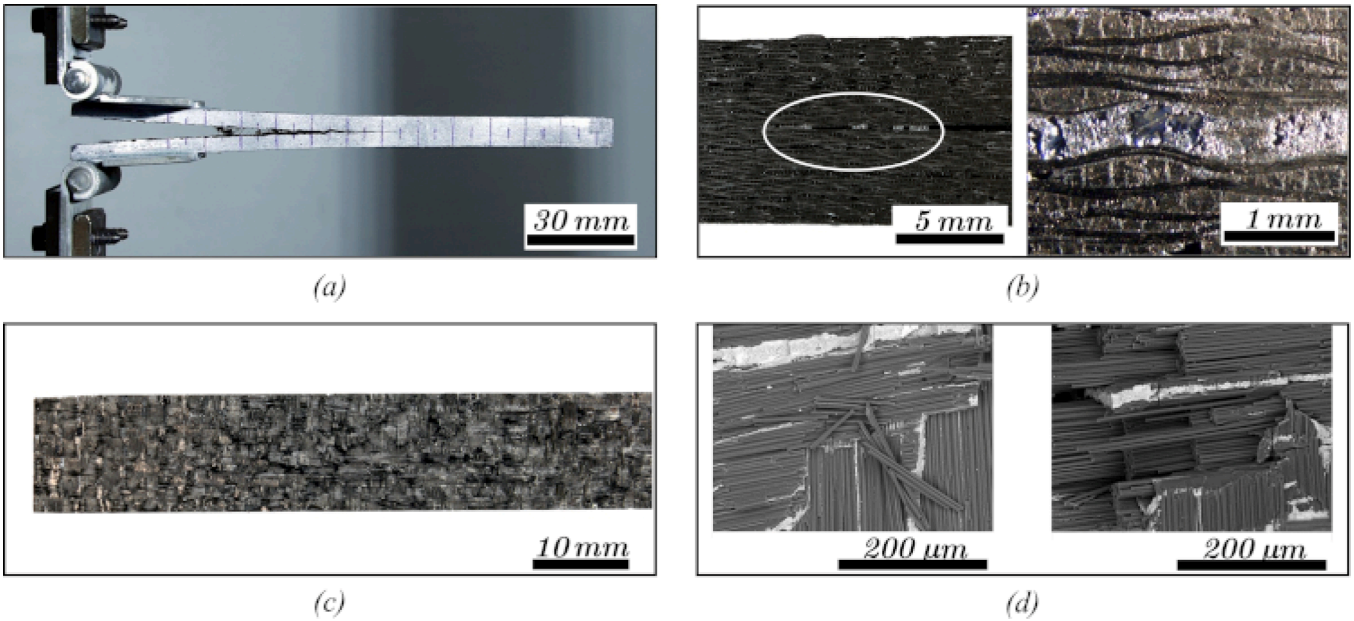

Fig. 1. first phase of DCB tests: (a) test configuration during the opening phase, (b) silicon accumulation in the pre-crack, (c) surface created by crack propagation, and (d) magnification of fiber damage in the yarns.

Every test was anticipated by a pre-opening, as prescribed in the standard, in which the crack was opened to the very first crack propagation. The pre-opening was performed to guarantee a natural morphology of the crack tip.

2.3. Results of the first test campaign

Four specimens were involved in the first test campaign, with samples named *A1*, *A2*, *A3*, and *A4*. All the specimens except *A2* showed high peaks of force in the very first millimeters of displacement during the pre-opening. These peaks are exemplified with the response of specimen *A3* reported in Fig. 2a, which reports the complete force (F) vs. displacement (δ) curve acquired in the tests, including the pre-opening. The complete response of *A2* specimen, which did not exhibit the peak, is also presented. The other curves exemplify typical responses, including the pre-opening, of the specimens adopted in the second phase of the test campaign, which will be described in the next sub-section. The force peak of specimens *A1*, *A3*, and *A4* was interpreted as a consequence of the discrete connections originated by the silicon accumulation between the pre-cracked faces, which required the application of high force level to fail and to completely develop the pre-crack. The relationship between these force peaks and the presence of silicon is confirmed by the analysis of the pictures taken during the pre-opening, which indicate that the opening was opposed by discrete connections until the occurrence of the force peak. After the pre-opening the specimens were unloaded and the responses in the subsequent opening phase were quite similar to those expected in a DCB tests on polymeric matrix composites (see for instance [28,29]), as it is shown in Fig. 2b, where all the response of the specimens involved in the preliminary campaign are presented, without including the pre-opening phase. However, the response is characterized by a progressive deviation from linearity before the force peak, which indicate a smooth progression of inelastic processes in the specimens and by some irregularities in the softening phase. The scattering is not negligible since the difference between the curves can reach values of about 20% of the average maximum force levels.

Cracks tended to develop along a straight path, although the detachment of fibers from the yarns of the carbon fabric reinforcement is apparent in Fig. 1a and produced some irregularities in the propagation direction. Such damage, with the bundles of broken fibers raised from the surfaces, was clearly visible on the surface created by crack propagation, shown in Fig. 1c, which was taken on a specimen completely split during the DCB tests. The magnification shown in Fig. 1d, taken at the SEM microscope, indicates that both the yarns in the longitudinal and in the transverse direction are involved in this fiber damage phenomenon. Actually, damage was found to be distributed between the longitudinal and transversal yarns, suggesting that it could not be completely attributed to the in-plane stress state acting on the arm of the DCB specimen, which is subjected to severe bending during the crack opening. However, in the *A3* specimen a neat crack jump from one interlaminar to the adjacent one occurred after an opening of about 8 mm. Such crack deviation led to the bending failure of one of the arms and to the premature termination of the test.

A preliminary quantitative estimation of the toughness was done by applying the Modified Beam Theory (MBT) data reduction method, which is one of the approaches suggested by the standard [27]. The resultant toughness versus crack length curves indicate a clear R-curve effect, with a value of toughness that tends to increase with the increasing crack length, which is visible in Fig. 3, where G_c indicates the toughness and a the crack length, and could be related to the development of a damage zone at the crack tip. Considering the visual analyses reported in Fig. 1, fiber bridging and fiber damage are likely to play an important role in the development of the damage zone. The general trend suggests that an asymptotic value of about 0.40 kJ/m^2 can be observed. Such value is reached after different crack propagation length for the different specimens. Although the toughness values exhibit significant irregularities during all the crack propagation phase, a crack length for the establishment of a regime close to steady state

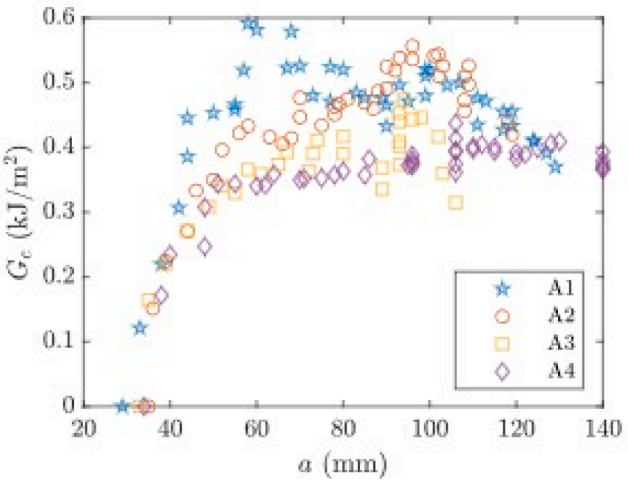

Fig. 3. critical energy release rate vs. crack length measured in the first phase of DCB testing.

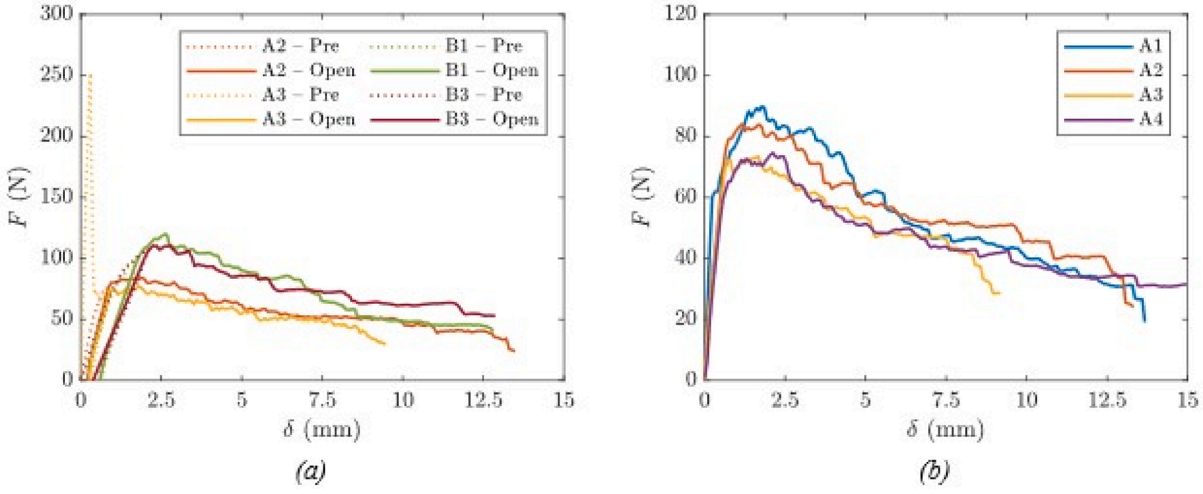

Fig. 2. force vs opening curve showing (a) force peak during the preopening for specimen *A3*, and (b) responses of the first batch of specimen without preopening.

propagation can be identified in the range 30 ÷ 45 mm. Accordingly, the MBT method suggests the development of a significant damage zone, but, at the same time, confirm the scattering and the irregularities of the data among the different specimens and also within the response of the same specimen.

2.4. Results of second test campaign on thick specimens

A new batch of DCB specimen was produced with an increased thickness with the aim of reducing the level of the in-plane stress components due to bending, so that the comparison with the previous tests could provide an indication of the possible influence of bending stress on the measured interlaminar toughness. Moreover, the method to produce the pre-crack was improved by applying Boron Nitride, which is used as a release agent for high temperature applications, to the PTFE stripes used to produce the pre-crack. This modification of the procedure allowed the production of specimen with longer pre-cracks, without geometrical distortion and no apparent discrete connections produced by silicon accumulations. With this technique three specimens were produced, named *B1*, *B2,* and *B3*, with a length of 196 mm, a width of 12.52 ± 0.11 mm and a thickness of 11.93 ± 0.04 mm. Thanks to the absence of pure silicon in the pre-cracked zone, the distance from the tips of the pre-cracks from the edge was more easily measurable and was evaluated to be about 80 mm. The longer pre-cracks allowed the bonding of the hinges in a configuration that respected the prescription of the standard, as shown in Fig. 4a, thus avoiding the potential stiffening effect of the metallic tabs of the hinges on the arm stiffness. The nominal pre-crack length, measured from the hinge axis, resulted to be 50 mm for all the three specimens. A comparison state of the pre-crack between the specimens produced for testing phases *A* and *B* is presented in Fig. 4b, taken after the complete opening and splitting of the two representative samples, which were placed with the pre-crack ends aligned. In the specimen above, which was taken from the first test campaign, the crack end is not easily identifiable, and the clear light-reflecting regions indicate the zone where silicon was able to penetrate in the pre-cracked region. In the specimen below, obtained with the process applied in the testing phase *B*, the boundary of the pre-crack is neat. The white material is the residual of the PFTE sheet protected by the release agent after pyrolysis and infiltration, but no silicon accumulations are present.

A pre-opening phase was carried out, which was interrupted when the crack length reached 55 mm, as measured by the scale drawn on the specimen side. The two examples reported in Fig. 2a, referred to specimens *B1* and *B3*, indicate that force peaks were eliminated in the pre-opening response. Due to the nature of the pre-opening phase, which did not show force peaks and was intentionally prolonged to obtain a crack propagation $\Delta a = 5$ mm, it was decided to consider the pre-opening as a part of the opening, in order to take into account the initial deviation from linearity of the response, as illustrated in Fig. 5a, which reports the responses of all the specimens included in this second test campaign, merging the pre-opening and the opening phase. The circle indicates the end of the pre-opening phase, indicating that a deviation from linearity and the consequent activation of inelastic mechanisms occurred also during the pre-opening.

The force–displacement curves obtained in the opening phase showed an acceptable repeatability, with a lower degree of scattering with respect to the test carried out on specimens *A*, as shown in Fig. 5a. The crack reached the end of the specimen in all the tests, without any flexural failure. Fiber damage along the crack path was present, as shown in Fig. 4a. Such phenomenon did not show significant differences with those documented in testing phase *A*.

2.5. Bending and tensile response of the material

The development of a numerical model of the specimens required an elastic characterization of the material. The elastic modulus in the longitudinal direction and the presence of in-plane inelastic response was evaluated by performing tests on five specimens in three-point bending configurations, following the standard ASTM C1341 [30]. A series of loading–unloading cycles performed to investigate the non-linear response of the material and flexural modulus of 55.85 GPa with a standard deviation of 7.92 GPa was evaluated.

The results showed a relevant degree of scattering especially in the values of flexural modulus. A little amount of non-linearity was found during the loading part of the cycles consistent with a residual deformation that was found at unloading. Such pseudo-plastic response resembles the trends shown in literature for CMC materials tested along fiber reinforcement direction, mentioned in the introduction. The results obtained from the experimental test were used to tune an equivalent elastic plastic material model, which represent the flexural behavior of the material. The model was developed to represent the macroscopic behavior of the DCB arms, without aiming at representing the true nature of the dissipative phenomena during bending, so that a very simple material model was adopted by implementing an isotropic elastic material, with the elastic modulus identified in bending, a yield surface based on Von Mises criterion and a tabular isotropic hardening. The tuning was verified by implementing a FE model of the three points bending test, which is reported in Fig. 6a, that allowed to ensure that the

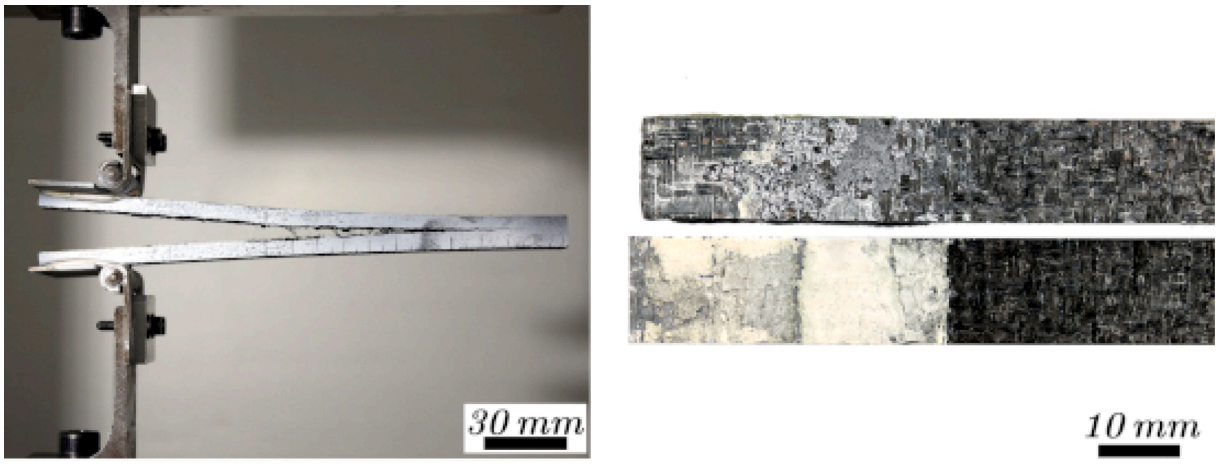

Fig. 4. second phase of DCB testing: (a) opening of specimen *B1* with broken fibers raised from the crack surface and (b) comparison of the pre-cracked surfaces between phase *A* and phase *B* specimens.

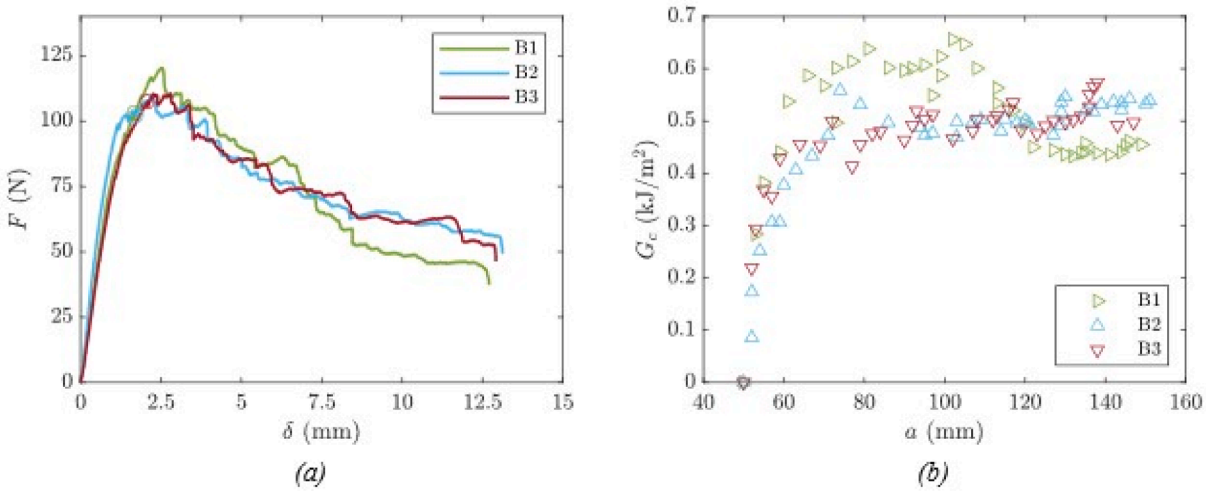

Fig. 5. second phase of DCB testing: (a) force vs. displacement responses and (b) critical energy release rate vs. crack length.

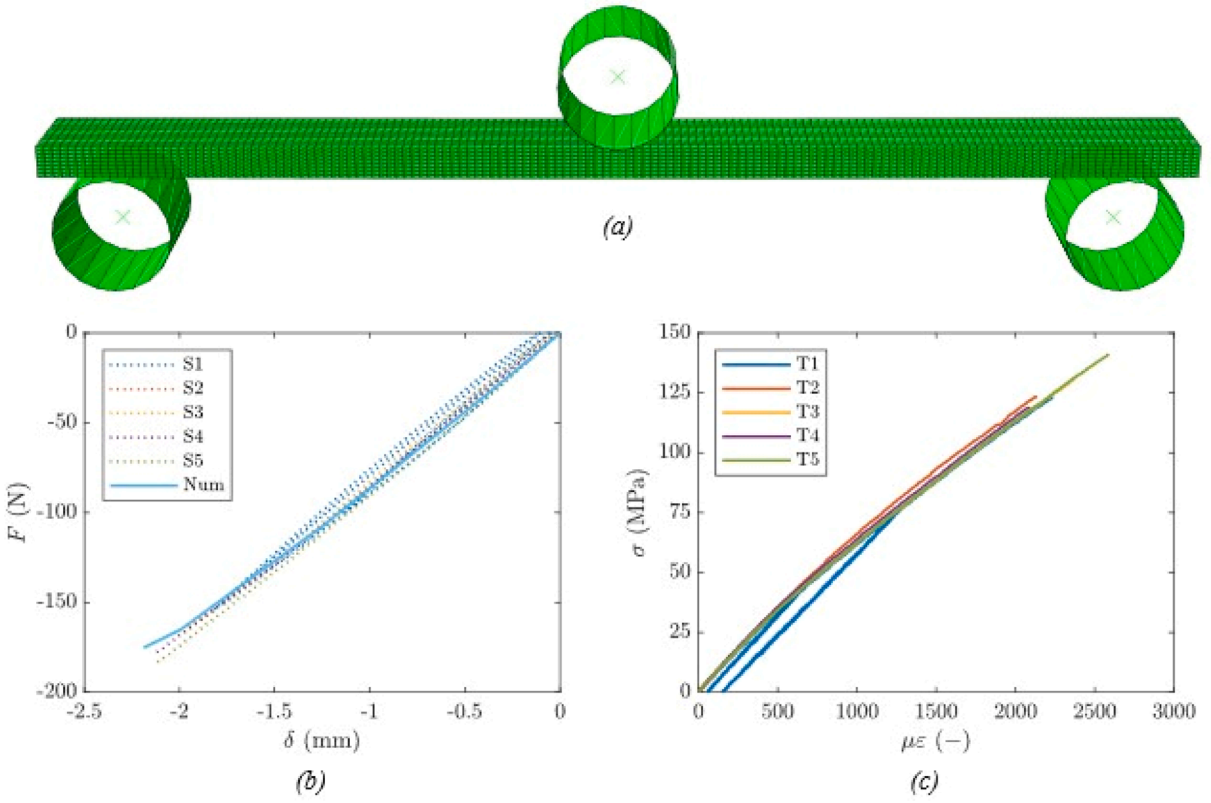

Fig. 6. (a) FE model of the 3pt bending test, (b) numerical experimental correlation of the elastic plastic material law in bending, and (c) tensile stress vs. strain curves.

identified values led to a good numerical experimental correlation, as shown in Fig. 6b, where F and δ have the same meaning as for the DCB responses of force and displacement, respectively.

A characterization campaign was also performed for tensile properties, which were evaluated by adopting the ASTM C1275 standard as a guideline [31], using dog-bone shaped specimens. The results, shown in Fig. 6c and reported as axial stress σ versus axial strain in microstrain $\mu\varepsilon$, confirmed a slightly non-linear response and indicated a tensile strength of about 120 MPa.

3. Development of a numerical approach

The experimental results reported in the previous section indicate that the interlaminar damage propagation is characterized by an R-curve, which is likely to be related to the occurrence of fiber damage and bridging. Results could have been influenced by the in-plane stress states in the plies during bending, by the non-linear response documented in bending tests, and by the occurrence of high peak forces in the pre-opening phase. However, the influence of all these factors was different in the preliminary tests and in the test campaign with thicker specimens. A numerical approach, based on the application of Cohesive

Zone Models, was developed to study, identify, and compare the interlaminar properties in all the tests performed, so to improve the reliability of the interface characterization and to make available a calibrated model for the analysis of delamination propagation in LSI-produced CMC material. The approach relied on the training of a Regression Neural Network, which was used to perform a Genetic Algorithm based optimization.

3.1. Tri-linear cohesive zone model

Cohesive Zone Models (CZM) have been adopted in many literature works to model the propagation of interlaminar cracks in polymeric as well as in Ceramic Matrix Composites [21,32]. They work by linking the displacement discontinuities at the interface with the tractions transmitted through the crack faces during a crack propagation process. The stress vs. traction law typically used has a triangular shape (bi-linear CZM) and is able to represent both the interface strength, represented by the height of the triangle, and the interface toughness, represented by area under the whole triangular response. CZM's are normally implemented in zero-thickness or infinitesimal thickness interface elements, referred to as Cohesive Elements, which are nowadays available in many commercial FE codes. An approach to obtain a numerical model to represent the R-curve effect was presented and adopted in [21,22,26,28] and relies on the implementation a trilinear cohesive law. In this method, the stress vs. traction response the CZM is obtained by using two bi-linear cohesive laws superposed, characterized by different toughness (G_1 and G_2) and different strengths (σ_1 and σ_2). The superposition leads to obtain a global response of the cohesive layer in terms of stress (σ) vs displacement (δ) as a trilinear law, as shown in Fig. 7, which is characterized by four parameters. Two of the four parameters represent the overall properties of the cohesive interface, being them G_c, the toughness of the steady state propagation after the development of the damage zone, and σ_c, which is the strength of the interlaminar layer. Two other parameters distribute such properties between the two superimposed bi-linear cohesive responses. These parameters are m, which defines the distribution of the toughness, as $G_1 = mG_c$ and $G_2 = (1-m)G_c$, and n, which determines the distribution of the strength, with $\sigma_1 = n\sigma_c$ and $\sigma_2 = (1-n)\sigma_c$. By varying the m and n parameters between zero and the unit value, the shape of the force vs. opening curve obtained in the DCB test is varied, as a consequence of a R-curve effect introduced in the interface response, which depends on the development of a damage zone before the steady state propagation phase [22,28,33].

Following the theoretical work presented in [22,26,34] it is possible to define the relationship between the tri-linear model and the length of the damage zone, which is presented in Eq. (1). Other than the four parameters of the trilinear law, the equation is function of the damage zone length ($l^{SS}_{c_{tri}}$), of the DCB arm thickness (t_{arm}), of elastic modulus (E_{11} for crack propagation direction and E_{22} for transversal direction), of in-plane shear modulus (G_{12}), of in-plane Poisson's ratio (ν_{21}), and of a coefficient γ. The equation already accounts for the fact that according to [34] the evaluation of the length of the damage zone requires an important correction factor related to the bending of the arms. The form of correction adopted was introduced in [26] and was validated for trilinear response. The coefficient γ can be set to 0.73, according to [35].

$$l^{SS}_{c_{tri}} = \left(t_{arm} \left(t_{arm} + \left[\frac{m^2}{n^2} + \left(\frac{1-m}{1-n} \right)^2 - \frac{m(1-m)}{n(1-n)} \right] \gamma \frac{G_c}{\sigma_c^2} E_{22} \left(\frac{1}{2} \sqrt{2 \left[\sqrt{\frac{E_{22}}{E_{11}}} - \nu_{21} \right] + \frac{E_{22}}{G_{12}}} \right)^{-1} \right)^{-1} \right)^{0.71} \tag{1}$$

This relation makes possible the development of an analytical method to find the parameter n, knowing m, which can be estimated as the ratio between the initial and steady state toughness, and $l^{SS}_{c_{tri}}$, which can be estimated knowing the R-curve resulting from MBT data reduction. In the current work, the relation was used to estimate the length of the damage zone, given the parameters m and n of the trilinear model, which were identified numerically through an automatic identification process based on the minimization of errors between the numerical and experimental force vs. opening responses.

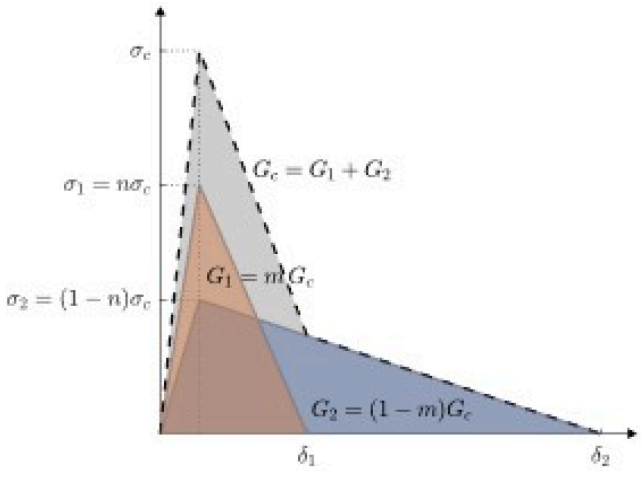

Fig. 7. superposition of two bilinear Cohesive Zone Models to obtain a trilinear traction separation law.

3.2. Finite element model of the DCB tests

A FE model of the DCB test was deployed to analyze the opening phases of all the tests performed by using the Simulia/Abaqus Standard code. The model had to integrate the double cohesive layer and was required to be computationally efficient, since it was intended to be used in an automatic identification algorithm involving a large amount of analysis. Finally, it needed to be as accurate as possible with respect to the real specimen and to the load-introduction method. Considering the need of representing specimens with different thickness and different pre-crack length after pre-opening, a parametric script was implemented, which was able to generate the input files for the FE. Moreover, the script included the possibility of introducing reversed hinges in the mesh, which could not be neglected in the specimens adopted in the first test campaign. The model developed had planar typical dimensions of the elements of 0.5 mm in the crack propagation direction and 2.0 mm in the transversal direction and was composed by about 2700 cohesive elements (*COH3D8*, [36]), 3500 continuum shell elements for the specimen, and 3000 for the hinges (*SC8R*, [36]). For the thick specimens used in the second test campaign, the hinges were eliminated in the model, since they were mounted as prescribed by the standards and could not influence the bending of the arms.

3.3. Automatic identification procedure

The approach used for the identification of the CZM parameters was

based on an automatic process focused on the force vs. opening response, analogous to the one presented in [26]. The procedure consists of different steps. At first, a set of numerical observation was created: each observation was obtained by adopting different values of the predictors, which were the variables to be identified, namely G_c, σ_c, m and n. To generate the observation set a Latin Cube Allocation algorithm [37] was used to obtain the coordinates of the observation points in the four-dimensional domain of the variables. For each observation, the DCB test was simulated, generating a database of numerical responses, in terms of reaction force F vs. the DCB arms displacement, δ. Following the approach presented in [26], the $F(\delta)$ curves obtained from the simulation were used to compute the error between numerical response and the experimental one. The discrepancy between the numerical force vs. opening response, $F_{num}(\delta)$, and the experimental one, $F_{exper}(\delta)$, was measured by dividing the curves in 3 regions, which were the elastic part, the transition region, and the steady state propagation up to $\delta = 7.5$ mm for batch A and $\delta = 10$ mm for batch B. For each region i the error was computed as Eq. (2), where $\bar{\delta}_k$ represents the starting value of δ for the region k and taking $\bar{\delta}_4$ equal to the final value of δ considered for each batch. The errors were combined as $e = \sqrt{\sum_{i=1}^{3} e_i^2}$ to obtain the global error e.

$$e_i = \frac{1}{\bar{\delta}_{i+1} - \bar{\delta}_i} \int_{\bar{\delta}_i}^{\bar{\delta}_{i+1}} \left| F_{num}(\delta) - F_{exper}(\delta) \right| d\delta \tag{2}$$

Thereafter, the database of the global errors was used to build a regression model to obtain a response function of the type $e(G_c, \sigma_c, m, n)$. The regression model implemented was a Regression Neural Network [38] which is available in the Statistics and Machine Learning Toolbox of MathWorks/Matlab® [39]. Such Toolbox was used for the training and verification of the model. The regression model was used to perform an optimization in order to evaluate the model parameters giving the minimum value of the error. Such optimization was performed by adopting a genetic algorithm [40], which is implemented in Global Optimization Toolbox of MathWorks/Matlab® software package [41].

4. Assessment of the numerical approach

The procedure illustrated in the previous section was aimed at the identification of the interlaminar properties for all the specimens involved in the tests. Before applying the procedure systematically, it was applied considering a first case, which acted as the benchmark and was used to evaluate the approach effectiveness in representing the interlaminar fracture response, the development of the damage zone during crack propagation, its limitation, and the potential effects of bending non-linear response.

4.1. Application of the identification procedure to a specimen and analysis of the results

The first trial of the identification approach was carried out on specimen *A1*. An initial tuning of the model was required to capture the slope of the $F(\delta)$ curve in the initial elastic phase of the response, which is affected by several factors: the exact position of the crack tip, difficult to be measured as documented in Fig. 4b, the scattering of the stiffness moduli exhibited in the bending tests, and the influence of the hinges. The material was characterized considering a homogeneous lay-up of isotropic plies, with Young modulus $E = 55848$ MPa and Poisson's ratio $\nu = 0.01$. The model included the reversed steel hinges, which were modelled by assuming a modulus $E = 200$ GPa and $\nu = 0.3$. An initial crack length of $a_0 = 32.0$ mm was identified to match the initial slope of the $F(\delta)$ curve. The value is not very different from the one used in the data reduction for the *A1* specimen (see Fig. 3) and was deemed to be acceptable.

After this tuning, the observation set was created by defining reasonable ranges for the predictors. The results of the data reduction for the tests in the first campaign, reported in Fig. 3, provided clear indications for the ranges of G_c and for the m parameter, which is the ratio between the initial and the asymptotic value of the toughness. The range for the n parameter was taken similar to the one adopted in [26]. The choice of a proper value for σ_c would require specific tests for interlaminar strength, since the DCB tests are specifically designed to measure just the interlaminar toughness and are generally insensitive to the strength values. The range was chosen considering that the LSI-produced CMC should not achieve very high mechanical strength for properties completely dominated by the matrix. However, the procedure was not expected to obtain precise indications regarding the σ_c value. These considerations led to the following choices for the ranges of variability of the predictors, which were taken as: $0.25\,\text{kJ/m}^2 \le G_c \le 0.45\,\text{kJ/m}^2$, $15\,\text{MPa} \le \sigma_c \le 30\,\text{MPa}$, $0.075 \le m \le 0.5$, and $0.75 \le n < 1.0$. The total number of observations was set to 1000. The first trial of identification suggested to densify the observation set in the region of high n values, where the error showed a strong dependency from n, to improve the quality of the results. Fig. 8 reports the evaluation of the error for increasing n for all the observations, with different values of the other predictors. The plot confirm that the error showed a general tendency to decrease as the value of n increases until the reach of a minimum point, around $n = 0.95$. However, after this minimum the error tends to increase rapidly having its maximum for $n \approx 1$.

Accordingly, the high density of points around $n = 0.95$ can be considered a requirement to build a regression model capable of representing with adequate accuracy the minimum valley, where the optimal solution was located. For such a reason, only 150 observations were performed with $0.75 \le n < 0.85$, whereas the remaining 850 observation were conducted in the range $0.85 \le n < 1.0$. Eventually, 929 valid observations were obtained, discarding some analysis that showed convergence problems and were far from optimal point. Two subsets were created and used to train (500 observation) and test (429 observation) the Neural Network to improve the identification by means of an optimization process. The Regression Learner application available in MathWorks/Matlab® code [39] allowed to train and test different regression schemes and provided comparison between the networks in terms of Root Mean Square Error (RMSE). To validate the training accuracy a 10-fold cross validation method was adopted [39]. All the regression schemes trained presented the tendency to increase their residual as n increase above 0.95, which was expected due to the presence of the steep fitting valley, but none of them showed signals of overfitting, with RMSE for validation and for testing showing

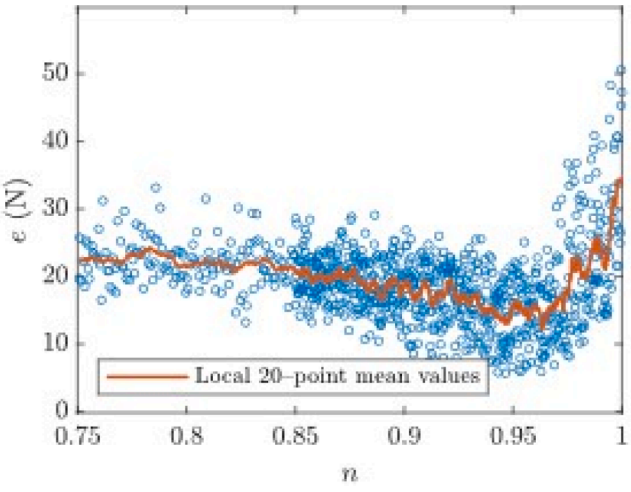

Fig. 8. error for the different observation ordered for n on the abscissa. The fitness valley can be identified around $n = 0.95$.

Table 1
identified properties for specimen *A1* adopting different strategies.

	G_c(kJ/m^2)	σ_c(MPa)	m	n	e_p(N)	e_c(N)	$l_{c_{ini}}^{SS}$(mm)
Best Fitting Solution	0.438	24.96	0.123	0.947	5.66	5.71	37.7
Optimized Solution	0.441	25.42	0.225	0.965	5.30	5.55	44.3
σ_c = 17.5 MPa	0.433	17.5	0.189	0.931	6.55	6.53	37.7
σ_c = 20 MPa	0.446	20.0	0.194	0.957	5.59	6.21	46.3
σ_c = 25 MPa	0.439	25.0	0.133	0.956	5.33	6.26	41.7
σ_c = 27.5 MPa	0.437	27.5	0.242	0.968	6.26	6.00	43.9

comparable values. In the end, the neural network that was selected was composed by one fully connected layer with 100 hidden nodes and activation function of the type ReLU (Rectified Linear Unit) [39]. The regression model obtained was then used in an optimization process using the genetic algorithm available in MathWorks/Matlab® [41], taking the four predictors as variables and using as domain for the population the four-dimensional domain containing them. The optimal was obtained with a population size of 50, a crossover fraction of 0.8 and an elite count of 3. The parameters of the Optimized Solution that were obtained are reported in Table 1. The error of the Optimized Solution is not dissimilar from the error obtained by the set of predictors that achieves the lower error among all the sets used to build the regression model. The latter set of parameters is reported in Table 1 as Best Fitting Solution.

The analysis of the population and different runs of the optimization indicate that several solutions exist with very similar error index, different values of the predictor σ_c, and similar values for the other three predictors. This fact confirmed that σ_c could not be identified through the process and led to repeat the optimization constraining the value of σ_c to four levels: σ_c = 17.5 MPa, σ_c = 20 MPa, σ_c = 25 MPa, and σ_c = 27.5 MPa. For such procedures, a unique solution was found. The obtained results are reported in Table 1.

The results obtained were verified by directly simulating the DCB with the identified parameters, in order to compare the error predicted by the Neural Network (e_p) with the error computed from the numerical response (e_c). The model performances were deemed as satisfactory in terms of the prediction quality, as indicated by the levels of e_p and e_c, which are very close, and confirmed by the direct comparisons of the experimental and the different numerical curves, shown in Fig. 9.

The overall toughness levels G_c identified for the different solutions are very similar, since they vary from 0.433 kJ/m^2 to 0.446 kJ/m^2, while more differences can be observed for the other parameters. In Fig. 9, it can be seen that the tri-linear cohesive model captures the deviation from linearity before the force peak for all the values of σ_c adopted and provides a good estimation of the maximum force. The differences between the identified solutions are concentrated on the first part of the response, whereas the softening phase is identical for all the simulation. However, the softening phase is also characterized by the maximum discrepancies with the experimental curves, thus indicating that the tri-linear cohesive model with a uniform characterization along the interface is not completely adequate to capture all the irregularities of the response, which are likely to be related to variation in the material structure at the micro- and meso- scale levels.

Eq. (1) was applied, considering the mechanical and geometrical properties reported in previous sections, to estimate the length of the damage zones corresponding to the identified tri-linear cohesive response. The corresponding damage zones length evaluated according to the semi-analytical procedure varies between 37.7 mm and 46.3 mm, as reported in Table 1, thus being in acceptable agreement with the results of the data reduction reported in Fig. 3. The small difference between the Best Fitting Solution and the Optimized Solution indicate that the regression model did not provide significant improvement with respect to the identification that could be obtained through a simpler Monte-Carlo approach. Although this depends on the high density of the observations in the fitting valley, it is remarked that such densification was actually required to obtain a reliable regression model.

4.2. *Influence of non-linear bending response*

The availability of an identification of the model parameters gives

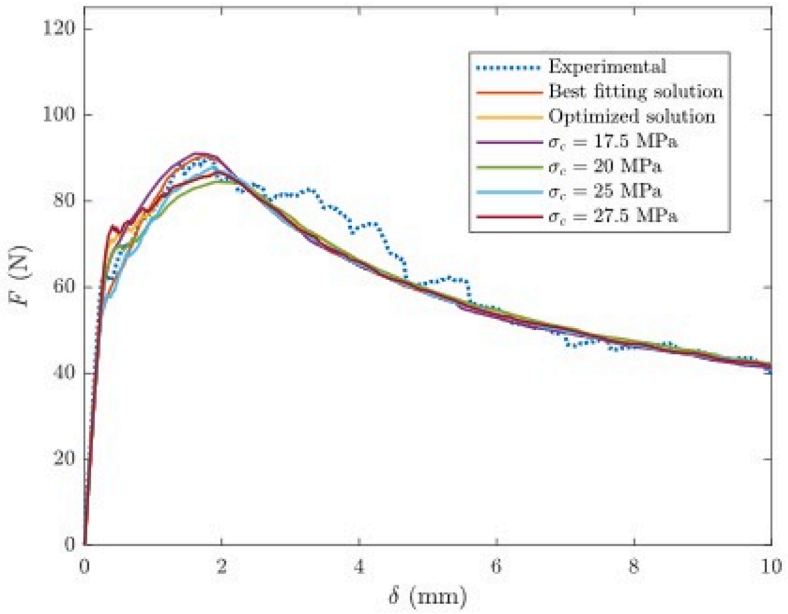

Fig. 9. comparison of the numerical responses obtained using predictor values identified through different strategies for specimen *A1*.

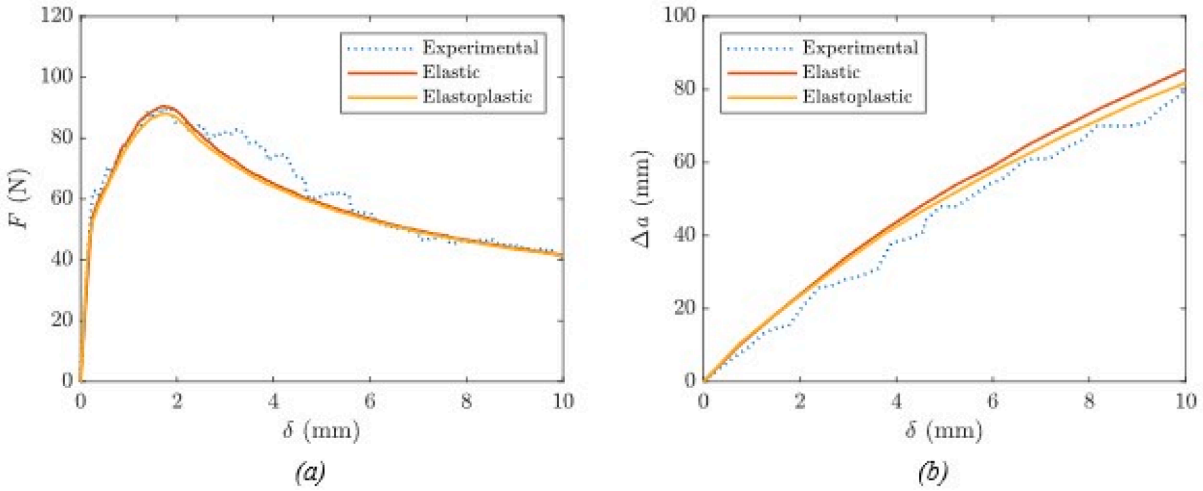

Fig. 10. response obtained with identical interlaminar properties and different material properties: (a) force vs displacement, (b) crack propagation vs displacement.

the opportunity to check the influence of the non-linearities of the material in bending, documented in the experimental tests. This effect could have led to a wrong estimation of the toughness, if the identification is based on the $F(\delta)$ response obtained using a linear behavior of arms, since the non-linear overall response of the DCB was exclusively attributed to the inelastic dissipation mechanisms involved in the crack propagation, without considering the contribution due to material non-linearity. For this reason, the simple plasticity model presented in Section 2.5 was integrated in the model of the DCB specimen *A1* and the results were compared with the ones obtained considering a purely elastic model. In both the simulations with the elastic and the elastic plastic laws, the previously identified parameters of the best fitting solutions were adopted for the tri-linear cohesive models. The force–displacement responses of the DCB with elastic and elastoplastic material are reported in Fig. 10a, where it can be seen that force vs. displacement curves obtained are almost identical. However, the predicted crack advancements (Δa) exhibit a difference of 5% between the two models, as shown in Fig. 10b. The advancement obtained with the elastic–plastic model is lower than the one referred to the elastic model and is closer to one measured in the experiments, which is affected by a significant uncertainty due to the difficulty in the detection of the crack tip.

It is worth noting that the comparison between Fig. 10a and Fig. 10b indicates clearly that crack propagation starts before the peak in the force vs. displacement response, which is in agreement with the progressive development of a damage zone and a critical energy release rate that tends to increase with the crack advancement.

4.3. Conclusions of the assessment process

The numerical studies performed considering the *A1* test, provided important indications regarding the reliability, the limitations, and the numerical effectiveness of the approach, which can be summarized in the following points:

- the trilinear cohesive zone model was found adequate to capture the basic features of the force vs. displacement responses, including the deviation of linearity, the peak of force and the steady state propagation, although some irregularities of the curves cannot be represented with a uniform distribution of interlaminar properties in the model;
- crack propagation is characterized by the development of a damage zone, with a length that can be predicted by the trilinear cohesive zone models at values consistent with the ones deriving from the R-curve obtained by data reduction;
- the DCB tests response appear to be uncorrelated with the values of the interlaminar strength σ_c, which cannot be identified through the automatic procedure;
- the identification process based on the Neural Network regression provides correct results, but it required a significant densification of observation in the fitting valley, so that it can be effectively substituted by a simpler Monte-Carlo approach;
- the influence of non-linear material response is small, though not completely negligible, and can be easily accounted for in the numerical approach, thus suggesting the inclusion of such aspect of the response it in the following systematic application to the whole set of experimental data.

5. Identification of the interlaminar model parameters in the tests and average values

The numerical approach, including modelling and identification, was systematically applied to all the specimens of both *A* and *B* batches. Seeing the conclusion of the assessment procedure, the material was considered elastic–plastic and the interlaminar strength was fixed to $\sigma_c = 20$ MPa. Moreover, a simple Monte-Carlo approach was adopted by properly densifying the database, computing the global error for the different observations, and choosing the best fitting one, without the build-up of the regression model and the subsequent optimization.

5.1. Results of identification procedure on the specimens of the first test campaign

In the first test campaign, the uncertainties in the crack position after the pre-crack, the presence of the hinges, and the scattering in the bending moduli required an initial tuning to precisely represent the elastic part of the response. As in the benchmark case, the tuning was focused on the identification of a crack length, by adopting an average value of the material Young modulus. It is remarked that this approach attributes to the initial crack length also the variation originated by the

Table 2
identified properties for the specimen batch *A*.

	a_0(mm)	G_c(kJ/m^2)	m	n	e_c(N)	$l^{SS}_{c_{ini}}$(mm)
A1	32.0	0.446	0.194	0.957	6.21	46.3
A2	38.0	0.421	0.483	0.937	5.68	27.7
A3	39.0	0.345	0.365	0.960	3.64	38.8
A4	38.0	0.353	0.353	0.951	3.99	35.0
*A**	36.8	0.391	0.349	0.951	–	36.4

scattering of bending stiffness, which was found significant in Section 2.5. However, all the crack lengths evaluated numerically were compared with the values derived from visual observations and adopted for the experimental data reduction reported in Fig. 3, to ensure that the values obtained were reasonable.

The observation set size was reduced with respect to the one used previously, since one of the predictors was fixed ($\sigma_c = 20$ MPa). For all the specimens the set of observation used was defined as $0.25 \leq G_c \leq 0.45$ kJ/m^2, $0.075 \leq m \leq 0.5$, and $0.75 \leq n < 1.0$. The total number of observations was of 500, with 50 of them with $0.75 \leq n < 0.85$ and 450 with $0.85 \leq n < 1.0$. The results of the identification via Monte-Carlo approach are reported in Table 2. For completeness, also the results already presented for the specimen *A1*, using $\sigma_c = 20$ MPa, are reported, although they were obtained by applying the optimization procedure with the regression model.

The $F(\delta)$ responses are reported in Fig. 11a, where the dotted lines represent the experimental curves, while the solid lines the numerical responses with the identified parameters. It can be observed that the specimen *A1* presents the lower initial crack-length and the most apparent deviation from linearity before the force peak. In the identification, these aspects led to the lowest m value and the highest estimate damage zone length. The value of G_c, as expected, regulates the steady state propagation and has an apparent influence on the final part of the response. After the development of the damage zone, the responses for *A1*, *A2*, *A3*, and *A4* are similar in pairs, the first one with a G_c between 0.42 kJ/m^2 and 0.45 kJ/m^2 while the second one with a G_c of about 0.35 kJ/m^2. In general, the responses obtained were able to capture the experimental ones with an acceptable correlation, considering the limitation involved in the adoption of constant properties along the crack path. Hence, the approach could not represent phenomena that were likely to be related to material inhomogeneity, as, for example, the apparent toughness growth in *A1* for δ between $\delta = 3$ mm and $\delta = 5$ mm, which is confirmed by data reduction in Fig. 3. It should be observed that the material inhomogeneity is also indicated by the scattering between the force levels and the shapes of the different curves, which is not negligible, and is reflected by the variation of the coefficient identified for the tri-linear model, presented in Table 2.

In the attempt to define a mean material model, the identified parameters were averaged, as well as the crack lengths and the specimen dimensions, to obtain an ideal average specimen, consistently with the decision to use the average material properties. This ideal average specimen was denoted as A^* and its material properties are included in Table 2. The response of A^* was numerically evaluated obtaining the response reported in Fig. 11b, which resulted in a behavior similar to *A4*, due to the similar values of m and n, but shifted to higher values of forces, due to the higher G_c. The response of A^* can be considered as representative of specimen batch *A*, being placed in region between the highest and the lowest experimental response over the whole range of δ. Accordingly, the interface model obtained by averaging the identified parameters from the separate specimen provided an acceptable mean model for the interlaminar response of the material.

5.2. Results of identification procedure on thick specimens

In the second batch of specimens the identification was performed over the whole response including the pre-opening, for the reasons stated in Section 2.4. The experimental results showed a certain amount of scattering in the elastic region, visible in Fig. 5a. Since the crack length could be more easily measured and controlled, this scattering was represented by varying the material elastic modulus. As in the case of batch *A*, the representation of the scattering by using a single parameter is a simplification, since some contributions could have been originated by the small differences in thickness and width of the specimens as well as small uncertainties in crack position. All the specimens required a tuning of the value of elastic stiffness, as reported in Table 3, with specimen *B2* requiring an increase in the value, while *B1* and *B3* a decrease. All the identified values were found in the interval $E = \mu_E \pm 1.75\sigma_E$, with the mean value ($\mu_E$) and standard deviation (σ_E) identified in the experimental bending tests and can be considered as acceptable. The observation set used was composed by 500 observations for *B2* and by 1000 observations for the other two specimens, due to a required expansion of the boundaries for the G_c predictor. The boundaries of the set were defined as follows: 0.35 kJ/m^2 $\leq G_c \leq 0.50$ kJ/m^2 for *B2* and $0.35 \leq G_c \leq 0.65$ kJ/m^2 for *B1* and *B3* while m and n respects the previous limits and, for n, also the ratio for the distribution in the interval.

The identified parameters, reported in the Table 3, were similar for specimens *B1* and *B3*, which presented a similar shape of the responses. The higher error found for the best fitting curve of *B1* derives from the

Table 3
identified properties for specimen batch *B*.

	E (MPa)	G_c (kJ/m^2)	m	n	e_c (N)	$l_{c_{ini}}^{SS}$ (mm)
B1	43,500	0.565	0.314	0.879	7.07	28.6
B2	60,000	0.469	0.370	0.962	3.71	56.1
B3	42,000	0.523	0.272	0.885	3.32	29.7
*B**	48,500	0.506	0.276	0.904	3.05	34.2

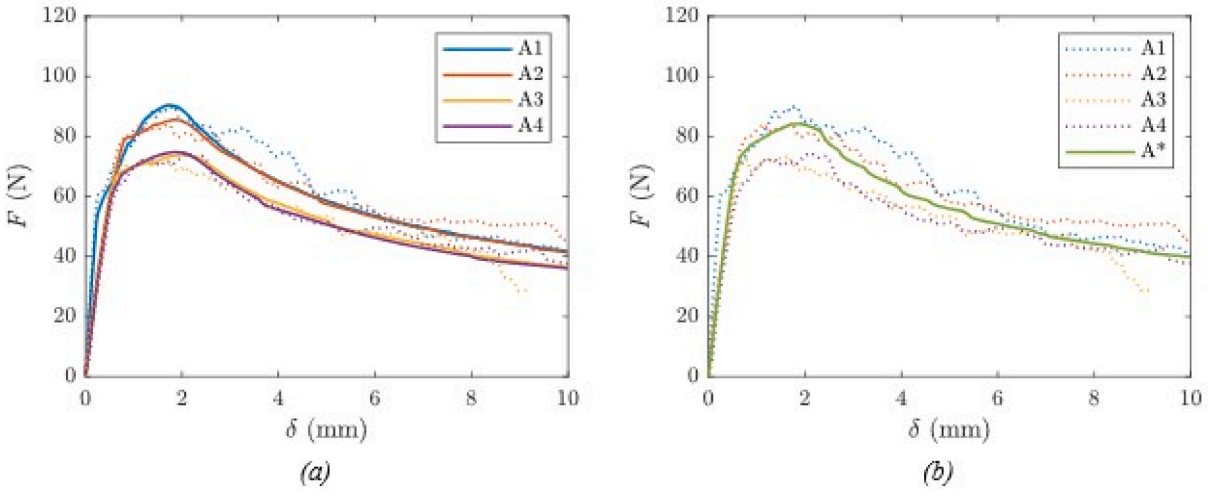

Fig. 11. (a) numerical DCB response using the identified properties for specimen batch *A* compared with corresponding experimental responses. (b) numerical response of the fictional average specimen (A^*) compared to experimental responses.

apparent reduction of the toughness in the final part of the response, which is recognizable also from the values of G_c identified by the MBT, reported in Fig. 5b. The experimental response of specimen *B2* was different from the other two specimens, showing a plateau at around 100 N for δ between 1 mm and 4 mm. This, led to identify a different pair of m and n giving an estimated damage zone longer than the one identified for *B1* and *B3*, at 50 mm, as was expected by looking at the MBT results.

To evaluate a representative set of values for the batch an additional identification was performed, using as reference a mean experimental curve, which was evaluated by interpolating the response of the *B1*, *B2*, and *B3* specimens at fixed values of δ, and averaging for each interpolation point the three force levels. The obtained response, denoted as B^* in Fig. 12, resembles the response of *B3*. The corresponding mean specimens was modeled by using the average dimensions of all the specimens in the batch *B*. Such numerical model was used to perform an identification of the material properties. The identified elastic modulus and interlaminar properties are reported in Table 3. The parameters identified for B^* are, as expected, similar to the ones obtained for *B3*. The parameters identified for B^* can be considered as a representative characterization for batch *B* specimens.

5.3. Comparison of thin and thick specimens identification results

The application of the identification procedure to all the specimens of batches *A* and *B* in the presented test campaign confirmed the conclusions achieved at end of the procedure assessment in Section 4.3. For a further discussion of the results, the visual representation reported in Fig. 13 can be used as a guide. In the plot, the material parameters referred to the two batches are listed along the x-axis (for example G_c^A is the toughness for batch *A*), while the corresponding normalized values are reported in the y-axis, with the normalization reference value given by the average value between the A^* and B^* representative characterizations. In such a way, the different number of specimens in the two batches is irrelevant and the variation with respect to the global mean values is immediately evidenced. For each parameter of the batches *A* and *B* the mathematical average value is reported, together with the upper and lower levels obtained in the individual specimens. Moreover, the values referred to the mean characterization A^* and B^* are also indicated.

The G_c values for the *A* type and *B* type specimens present similar scattering, with, average values that are very close to those obtained for the corresponding representative specimens A^* and B^*. The increment of toughness from *A* type to *B* type is apparent. On the other hand, m values and $l_{c_{tri}}^{SS}$ (reported for simplicity as l_c^A and l_c^B for batch *A* and *B* respectively) values are affected by large scattering. The scattering in m values probably depend on the local properties in the initial zone of crack propagation, which can provide initial values of toughness that can be far or close to the asymptotic steady state value, influencing the shape of the tri-linear cohesive response and, consequently, the length of damage zone. Despite the large scattering, an average value for the length of the damage zone, which is not so different from the values obtained for the representative curves A^* and B^* can be identified. The average length of the damage zone results 36.96 mm for the batch *A* and 38.12 mm for the batch *B*, while the corresponding value for A^* and B^* are 36.40 mm and 34.19 mm respectively.

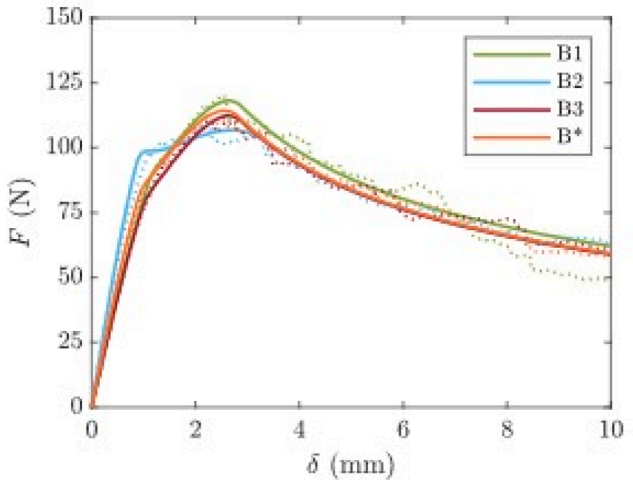

Fig. 12. force displacement response, for numerical (solid line) and experimental (dotted line) of specimen batch *B*, with the additional interpolated response and identification of specimen B^*.

It can be concluded that the inhomogeneity of the material properties affects both the response of the individual specimens, during the crack propagation process, and the scattering of the properties that can be identified for the specimen, considering the complete response of the DCB tests. However, the increment of toughness in the specimen of batch *B*, with respect to the ones of batch *A* seems not be related only to the scattering of material properties. The effect of the in-plane stress state of in the plies was investigated by evaluating and analyzing the state of stress at the crack interface. Such evaluation was performed by using a more complex DCB model, which included a solid element layer near the crack and was generated and calibrated according to the geometry and the material properties referred to the representative ideal specimens A^* and B^*. The maximum stress due to bending is expected to be constant during crack propagation, according to the application of Euler-Bernoulli beam theory and Irwin-Kies equation. Adopting such formulation for an isotropic material and considering a rectangular section, the definition for the DCB opening is reported in Eq. (3), where *B* indicates the specimen width.

$$\delta = \frac{8Fa^3}{EBt_{arm}^3} \tag{3}$$

The compliance can be defined as $C = \delta F^{-1}$ and the Irwin-Kies equation provides the definition of the energy release rate as $G = \frac{F^2}{2B}\frac{\partial C}{\partial a}$. Introducing the definition of compliance into the Irwin-Kies equation leads to Eq. (4)

$$G = \frac{12F^2a^2}{EB^2t_{arm}^3} \tag{4}$$

Inverting Eq. (4) to isolate the force F and substituting it into Eq. (5) the maximum tensile stress in bending (σ_b) can be written as function of the energy release rate, the elastic modulus, and the thickness of the arm as reported in Eq. (5).

$$\sigma_b = \frac{Fa\frac{t_{arm}}{2}}{\frac{1}{12}Bt_{arm}^3} = \sqrt{\frac{3GE}{t_{arm}}} \tag{5}$$

The crack propagates when $G = G_c$, and, considering an identical toughness, the expected reduction in the state of stress at crack propagation between A^* and B^* should be about 15%. In the numerical solutions, the increment of G_c in B^* attenuates such differences, as it is shown in Fig. 14, where the bending stress in specimens A^* and B^* resulted $\sigma_b^A = 104$ MPa and $\sigma_b^B = 96$ MPa, respectively, with a difference of 8%. It is worth noting that such values are quite close to the tensile strength of the material evaluated in the experimental tests reported in Fig. 6c, which is about 120 MPa. According to these simulations, a relevant bending stress level was achieved during the interlaminar crack propagation, comparable to the one required for the onset of fiber breakage in the yarns of the fabric. Since the breakage of fiber was observed as a typical phenomenon in crack propagation of both specimen type *A* and *B*, it is reasonable assuming that the lower stress level in the thicker *B*-type specimens led to an increment of the energy to be spent for the interlaminar crack advancement, which consequently

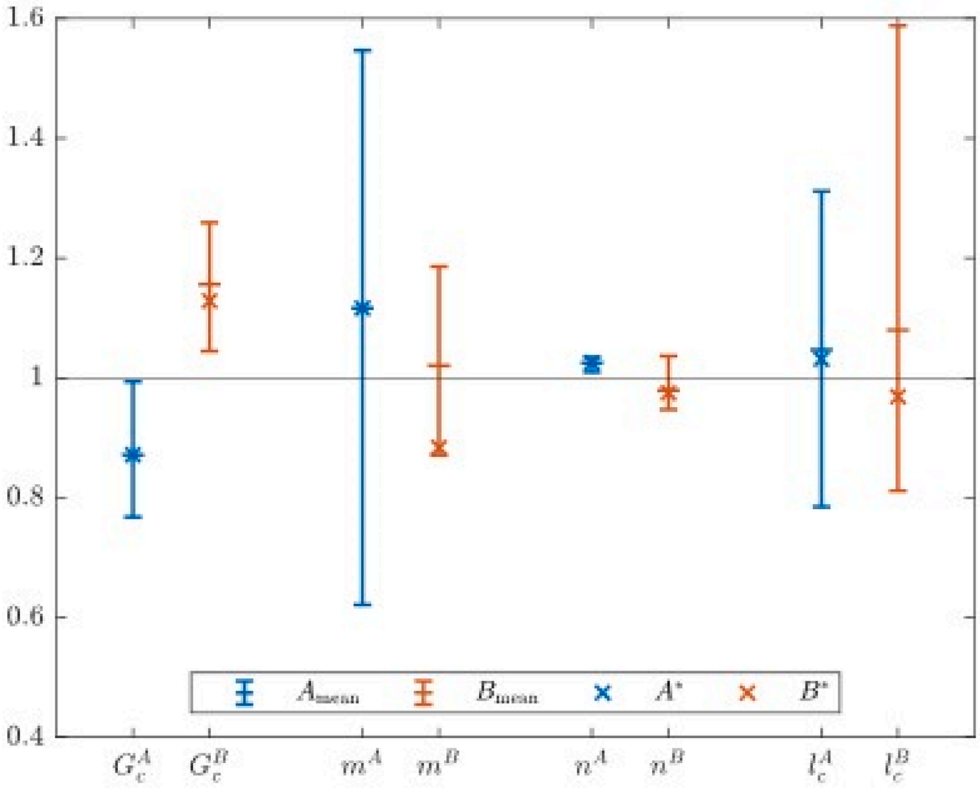

Fig. 13. mean value, scattering of the maximum and minimum identified value for each batch, A^* and B^* identified values. All values are normalized with respect to the mean value between A^* and B^*.

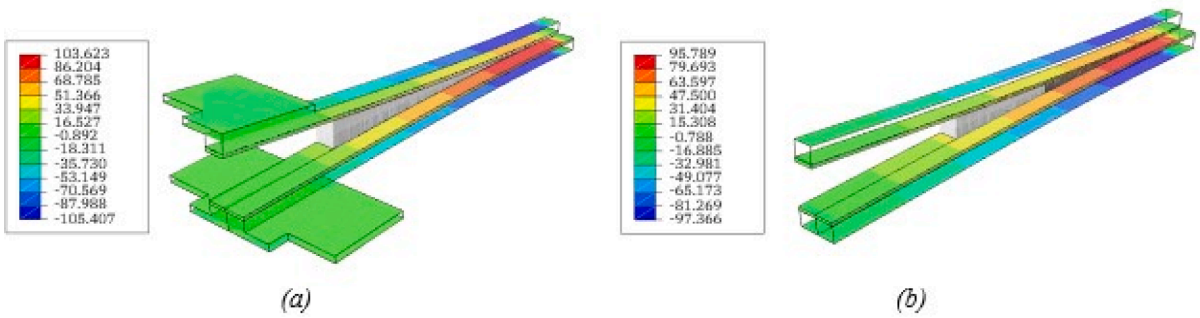

Fig. 14. peak in plane stress state at the crack interface for (a) specimen A^* and (b) specimen B^*.

increased the load required for crack propagation and the state of stress in the fibers. According to such interpretation, the interlaminar toughness in this LSI-produced CMC material has to be considered influenced by the in-plane stress state acting in the plies.

6. Conclusions

The LSI technology makes possible a reduction of the production cost of structural components made of CMC, in the field of space vehicles and propulsion. The investigation presented in this work has been aimed at achieving a quantitative and qualitative insight regarding the interlaminar response of LSI produced C/SiC fabric laminates, assessing an integrated experimental–numerical procedure for the characterization of such important aspect of the material, which is believed to be fundamental for the reliable design of structural elements.

The interlaminar response was found characterized by a noticeable R-curve effect, with an important increment of toughness during crack advance and a consequent improvement of the toughness and the damage tolerance of the material. Visual observations on two types of DCB specimens suggest that such effect is related to the development of damages in the fibers of adjacent plies, which are known to be weakened by the reaction with silicon during the infiltration process. The interface properties identified through conventional data reduction schemes and numerical identification approaches were characterized by significant scattering which can be attributed to material inhomogeneity and defects that affect both the crack propagation within the single specimen and the different mean properties that characterize the overall delamination process in different specimens.

In this context, the adoption of a non-mechanical method to produce the pre-crack allowed to carry out crack propagation experiments starting with sharp tips and propagating along a well-defined interface. The method, based on the interposition of a PTFE sheets covered by a chemical detaching agent provided very interesting results in the second step of specimens, which make it a promising approach to produce artificial defects in LSI-produced elements for damage tolerance experiments. The experiments have been integrated into a numerical

identification procedure, based on the implementation of 4-parameters tri-linear cohesive zone model and the minimization of the discrepancy between the numerical and experimental force vs. opening curves. The procedure proved to be capable of identifying the toughness and to capture the R-curve effect without any initial assumption on the parameters of the model. Moreover, the results were found not influenced by the value of the strength attributed to the interlaminar layer, which cannot be identified through a DCB test.

The numerical procedure was systematically applied to all the tests and used to extract mean responses that could be considered representative of the interlaminar layers. Two approaches were assessed successfully: the first based on the individual identification of the properties for each specimen in a batch, which have been subsequently averaged, and the second consisting in the evaluation of a mean curve that has been subjected to the identification process. The analyses of the mean responses showed also that the stress level due to the bending of the DCB arms were close to the tensile strength of the material. Such aspect could be related to the higher toughness evaluated by using thicker specimen, with a lower level on bending stress, since fiber breakage seems inherently involved in interlaminar crack advancement and a lower level of fibers stress leads to more energy required for crack advance.

Concluding, the integration of experimental observations on different specimens and of an effective numerical approach proved to be effective for understanding and characterizing the interlaminar response of the LSI produced C/SiC laminates providing important qualitative and quantitative data for the design of reliable and cost-affordable hot structures with such type of material.

CRediT authorship contribution statement

Marco Riva: Conceptualization, Methodology, Software, Investigation, Data curation, Writing – original draft, Visualization. **Alessandro Airoldi:** Conceptualization, Methodology, Formal analysis, Writing – review & editing, Supervision, Project administration, Funding acquisition. **Antonio Maria Caporale:** Investigation, Data curation, Writing – original draft. **Lorenzo Cavalli:** Conceptualization, Methodology, Resources, Supervision, Funding acquisition. **Mario De Stefano Fumo:** Conceptualization, Supervision, Funding acquisition.

Declaration of Competing Interest

The authors declare that they have no known competing financial interests or personal relationships that could have appeared to influence the work reported in this paper.

Data availability

Data will be made available on request.

Acknowledgements

Funding: This work was supported by the Italian Space Agency (ASI) as part of the project AM^{3}aC^{2}A: Multi-scale approach for modelling CMC and UHTCMC materials. We thank Matteo Boiocchi and Ahmed Afifi for the support during the experimental testing campaign.

References

[1] Krenkel W, Heidenreich B, Renz R. C/C-SiC composites for advanced friction systems. Adv Eng Mater 2002;4:427–36. https://doi.org/10.1002/1527-2648(20020717)4:7<427::AID-ADEM427>3.0.CO;2-C.
[2] Krenkel W, Berndt F. C/C–SiC composites for space applications and advanced friction systems. Mater Sci Eng A 2005;412:177–81. https://doi.org/10.1016/j.msea.2005.08.204.
[3] Patel M, Saurabh K, Prasad VVB, Subrahmanyam J. High temperature C/C–SiC composite by liquid silicon infiltration: a literature review. Bull Mater Sci 2012;35:63–73. https://doi.org/10.1007/s12034-011-0247-5.
[4] Hald H. Operational limits for reusable space transportation systems due to physical boundaries of C/SiC materials. Aerosp Sci Technol 2003;7:551–9. https://doi.org/10.1016/S1270-9638(03)00054-3.
[5] Glass D. Ceramic Matrix Composite (CMC) Thermal Protection Systems (TPS) and Hot Structures for Hypersonic Vehicles. 15th AIAA International Space Planes and Hypersonic Systems and Technologies Conference, Dayton, Ohio: American Institute of Aeronautics and Astronautics; 2008. https://doi.org/10.2514/6.2008-2682.
[6] Walker SP, Daryabeigi K, Samareh JA, Wagner R, Waters W. A Multifunctional Hot Structure Heat Shield Concept for Planetary Entry. 20th AIAA International Space Planes and Hypersonic Systems and Technologies Conference, Glasgow, Scotland: American Institute of Aeronautics and Astronautics; 2015. https://doi.org/10.2514/6.2015-3530.
[7] Bansal NP, Lamon J, American Ceramic Society, editors. Ceramic matrix composites: materials, modeling and technology. Hoboken, NJ: Wiley; 2015.
[8] Krenkel W. Cost Effective Processing of Cmc Composites by Melt Infiltration (Lsi-Process). In: Singh M, Jessen T, editors. Ceramic Engineering and Science Proceedings, vol. 22, Hoboken, NJ, USA: John Wiley & Sons, Inc.; 2001, p. 443–54. https://doi.org/10.1002/9780470294680.ch52.
[9] Hon MH, Davis RF. Self-diffusion of^{14}C in polycrystalline β-SiC. J Mater Sci 1979;14:2411–21. https://doi.org/10.1007/BF00737031.
[10] Gern FH, Kochendörfer R. Liquid silicon infiltration: description of infiltration dynamics and silicon carbide formation. Compos A Appl Sci Manuf 1997;28:355–64. https://doi.org/10.1016/S1359-835X(96)00135-2.
[11] Peng X, Zhuan L, Zi-Bing Z, Xiang X. The morphology and mechanism of formation of SiC in C/C-SiC composites fabricated by liquid silicon infiltration. J Ceram Process Res 2010;11:335–40.
[12] Lankford J. The failure of fiber-reinforced ceramic-matrix composites under dynamic loading. JOM 1995;47:64–8. https://doi.org/10.1007/BF03221181.
[13] Baste S. Inelastic behaviour of ceramic-matrix composites. Compos Sci Technol 2001;61:2285–97. https://doi.org/10.1016/S0266-3538(01)00122-1.
[14] Flores S, Evans AG, Zok FW, Genet M, Cox B, Marshall D, et al. Treating matrix nonlinearity in the binary model formulation for 3D ceramic composite structures. Compos A Appl Sci Manuf 2010;41:222–9. https://doi.org/10.1016/j.compositesa.2009.10.020.
[15] Hofmann S, Öztürk B, Koch D, Voggenreiter H. Experimental and numerical evaluation of bending and tensile behaviour of carbon-fibre reinforced SiC. Compos A Appl Sci Manuf 2012;43:1877–85. https://doi.org/10.1016/j.compositesa.2012.07.017.
[16] Hofmann S, Koch D. Predicting the mechanical behaviour of carbon fibre reinforced silicon carbide with interlaminar manufacturing defects. MATEC Web of Conferences 2015;29:00012. https://doi.org/10.1051/matecconf/20152900012.
[17] Kumar RS. Analysis of coupled ply damage and delamination failure processes in ceramic matrix composites. Acta Mater 2013;61:3535–48. https://doi.org/10.1016/j.actamat.2013.02.027.
[18] Kumar RS, Mordasky M, Ojard G. Delamination Fracture in Ceramic Matrix Composites: From Coupons to Components. Volume 6: Ceramics; Controls, Diagnostics, and Instrumentation; Education; Manufacturing Materials and Metallurgy, Oslo, Norway: American Society of Mechanical Engineers; 2018, p. V006T02A003. https://doi.org/10.1115/GT2018-75571.
[19] Airoldi A, Sala G, Bettini P, Baldi A. An efficient approach for modeling interlaminar damage in composite laminates with explicit finite element codes. J Reinf Plast Compos 2013;32:1075–91. https://doi.org/10.1177/0731684412473004.
[20] Hofmann S. Mode I delamination onset in carbon fibre reinforced SiC: Double cantilever beam testing and cohesive zone modelling. Eng Fract Mech 2017;182:506–20. https://doi.org/10.1016/j.engfracmech.2017.05.018.
[21] Kumar RS. Crack-growth resistance behavior of mode-I delamination in ceramic matrix composites. Acta Mater 2017;131:511–22. https://doi.org/10.1016/j.actamat.2017.04.012.
[22] Dávila CG, Rose CA, Camanho PP. A procedure for superposing linear cohesive laws to represent multiple damage mechanisms in the fracture of composites. Int J Fract 2009;158:211–23. https://doi.org/10.1007/s10704-009-9366-z.
[23] Abdel-Monsef S, Tijs BHAH, Renart J, Turon A. Accurate simulation of delamination under mixed-mode loading using a multilinear cohesive law. Eng Fract Mech 2023;284:109233. https://doi.org/10.1016/j.engfracmech.2023.109233.
[24] Ojard G, Barnett T, Dahlen M, Santhosh U, Ahmad J, Miller R. Mode I Interlaminar Fracture Toughness Testing of a Ceramic Matrix Composite. In: Singh D, Salem J, Mathur S, Ohji T, editors. Ceramic Engineering and Science Proceedings, Hoboken, NJ, USA: John Wiley & Sons, Inc.; 2010, p. 195–206. https://doi.org/10.1002/9780470944127.ch20.
[25] Kumar RS. Effects of randomly distributed defects on Mode-I interlaminar fracture of composite materials. Eng Fract Mech 2021;248:107699. https://doi.org/10.1016/j.engfracmech.2021.107699.
[26] Airoldi A, Dávila CG. Identification of material parameters for modelling delamination in the presence of fibre bridging. Compos Struct 2012;94:3240–9. https://doi.org/10.1016/j.compstruct.2012.05.014.
[27] D30 Committee. Test Method for Mode I Interlaminar Fracture Toughness of Unidirectional Fiber-Reinforced Polymer Matrix Composites. ASTM International. https://doi.org/10.1520/D5528_D5528M-21.
[28] Airoldi A, Baldi A, Bettini P, Sala G. Efficient modelling of forces and local strain evolution during delamination of composite laminates. Compos B Eng 2015;72:137–49. https://doi.org/10.1016/j.compositesb.2014.12.002.
[29] Ghiasvand S, Airoldi A, Bettini P, Mirani C. Analysis of residual stresses and interface damage propagation in hybrid composite/metallic elements monitored

through optical fiber sensors. Aerosp Sci Technol 2022;129:107373. https://doi.org/10.1016/j.ast.2022.107373.
[30] C28 Committee. Test Method for Flexural Properties of Continuous Fiber-Reinforced Advanced Ceramic Composites. ASTM International. https://doi.org/10.1520/C1341-13R18.
[31] C28 Committee. Test Method for Monotonic Tensile Behavior of Continuous Fiber-Reinforced Advanced Ceramics with Solid Rectangular Cross-Section Test Specimens at Ambient Temperature. ASTM International. https://doi.org/10.1520/C1275-18.
[32] Wisnom MR. Modelling discrete failures in composites with interface elements. Compos A Appl Sci Manuf 2010;41:795–805. https://doi.org/10.1016/j.compositesa.2010.02.011.
[33] Sorensen L, Botsis J, Gmür Th, Humbert L. Bridging tractions in mode I delamination: Measurements and simulations. Compos Sci Technol 2008;68:2350–8. https://doi.org/10.1016/j.compscitech.2007.08.024.
[34] Turon A, Costa J, Camanho PP, Maimí P. Analytical and Numerical Investigation of the Length of the Cohesive Zone in Delaminated Composite Materials. Mechanical Response of Composites, vol. 10, Dordrecht: Springer Netherlands; 2008, p. 77–97. https://doi.org/10.1007/978-1-4020-8584-0_4.
[35] Bao G, Suo Z. RemarkS ON CRACK-BRIDGING COncepts. Appl Mech Rev 1992;45:355–66. https://doi.org/10.1115/1.3119764.
[36] ABAQUS/Standard User's Manual, Version 6.14. Dassault Systèmes Simulia Corp.
[37] Mckay MD, Beckman RJ, Conover WJ. A comparison of three methods for selecting values of input variables in the analysis of output from a computer code. Technometrics 2000;42:55–61. https://doi.org/10.1080/00401706.2000.10485979.
[38] Specht DF. A general regression neural network. IEEE Trans Neural Netw 1991;2:568–76. https://doi.org/10.1109/72.97934.
[39] Statistics and Machine Learning Toolbox™ User's Guide, Version 12.1 (Release 2021a). The MathWorks, Inc.
[40] Goldberg DE. Genetic algorithms in search, optimization, and machine learning. Reading, Mass: Addison-Wesley Pub. Co; 1989.
[41] Global Optimization Toolbox User's Guide, Version 4.5 (Release 2021a). The MathWorks, Inc.